batteries

MDPI

Article

Interpretable Deep Learning Using Temporal Transformers for Battery Degradation Prediction

James Sadler *, Rizwaan Mohammed * and Kotub Uddin

Envision Energy UK COE Ltd., 27 Queen Anne's Gate, London SW1H 9BU, UK
* Correspondence: james.sadler@envision-energy.com (J.S.); rizwaan.mohammed@envision-energy.com (R.M.)

Abstract

Accurate modelling of lithium-ion battery degradation is a complex problem, dependent on multiple internal mechanisms that can be affected by a multitude of external conditions. In this study, a transformer-based approach, capable of leveraging historical conditions and known-future inputs is introduced. The model can make predictions from as few as 100 input cycles, and compared to other state-of-the-art techniques, our approach shows an increase in accuracy. The model utilises specialised components within its architecture to provide interpretable results, introducing the possibility of understanding path-dependency in Li-Ion battery degradation. The ability to incorporate static metadata opens the door for a foundational deep learning model for battery degradation forecasting.

Keywords: lithium-ion batteries; transformers; interpretable; deep learning

1. Introduction

Lithium-ion batteries have emerged as a cornerstone technology across multiple industries worldwide. Notably, they play a crucial role in the rapid advancement of electric vehicles (EVs) and large-scale battery energy storage systems (BESSs), two sectors that are pivotal to the transition towards sustainable energy solutions. For both of these applications, the associated Battery Management System (BMS) is responsible for optimising battery performance by managing parameters such as voltage, current, and temperature [1]. There is considerable motivation from researchers globally to improve the performance of BMSs [2], as they can extend battery life, reduce failure risks, and mitigate thermal runaway.

EVs rely heavily on efficient battery management to operate safely. The BMS is responsible for several critical functions, including temperature control, cell equalisation, charging and discharging management, and fault analysis. Effective battery state estimation, encompassing the State of Charge (SoC), state of health (SoH), and Remaining Useful Life (RUL), is vital for ensuring EV safety and performance [3]. Traditional estimation methods, such as the Kalman filter, often lack the adaptability needed to account for battery ageing effects, potentially compromising BMS performance [4].

In addition, BESSs are increasingly crucial in efforts to decarbonise the power sector. By facilitating the integration of renewable energy sources into the power grid, BESSs also contribute to grid stability and reliability. The BMS is vital to the viability of BESS projects. It is responsible for safety, the efficient management of performance, and determining the SoH of batteries. SoH predictions provide crucial information for the maintenance and replacement of batteries. Furthermore, trading strategies for BESSs must consider and optimise the SoH to balance short-term gains and long-term battery life.

Academic Editor: Zhenbo Wang

Received: 13 May 2025
Revised: 10 June 2025
Accepted: 18 June 2025
Published: 23 June 2025

Citation: Sadler, J.; Mohammed, R.; Uddin, K. Interpretable Deep Learning Using Temporal Transformers for Battery Degradation Prediction. *Batteries* **2025**, *11*, 241. https://doi.org/10.3390/batteries11070241

However, the gains generated by BESSs through providing flexibility services can be offset by the degradation cost of the lithium-ion batteries. In addition to lifetime and number of cycles, this degradation is sensitive to energy throughput, temperature, SoC, depth of discharge (DoD) and charge/discharge rate (C-rate) [5]. Furthermore, accurate state-of-health (SoH) estimation is crucial as it dictates the energy throughput, which determines the energy available for trading. This directly impacts the revenue generated from BESS projects and influences key financial metrics such as the Levelised Cost of Storage (LCOS) and Internal Rate of Return (IRR), ultimately governing the economic viability of these projects.

A major difficulty for SoH predictions in both EV and BESS applications is the inherent path dependency [6], i.e., the impact of the precise chronological usage of the battery on the SoH. Accounting for path dependency is not inherent to model-based methods—whether they are based on fundamental electrochemical equations [7–9] or circuit-based equivalent models combined with filtering techniques [10]—because path dependency is still not well understood. Moreover, capturing long-term SoH dependencies on the degradation stress factors mentioned previously within such frameworks require a large quantity of data to be collected over long periods of time, as demonstrated in Ref. [11].

A more efficient approach to SoH prediction is to employ data-driven methods [12] that can store and update key information from degradation data as they become available. Traditional data-driven methods for SoH prediction often involve handcrafted feature extraction followed by regression techniques. For instance, Feng et al. [13] used Gaussian process regression (GPR) and polynomial regression to predict SoH and RUL, extracting health indicators from charging current. These methods, while effective, can be time-consuming and labour-intensive, requiring expertise in feature design. Additionally, kernel methods, like support vector machines (SVMs), have been applied for SoH estimation [14]. However, selecting dominant data points can dilute path dependency and reduce prediction accuracy. Neural network (NN)-based techniques can be effective because they have an internal state that can represent path information.

The long short-term memory (LSTM) neural network architecture is a popular approach for time-series forecasting due to its ability to capture some long-term dependencies. Zhang et al. [15] studied LSTM-based neural networks for SoH predictions. Their results indicated that LSTM networks were generally more accurate and precise than SVM-based models. More recent studies have focused on end-to-end deep learning approaches using measurement data such as voltage, current, and temperature. Li et al. [16] combined LSTM and CNN networks to separately predict SoH and remaining useful life (RUL) in an end-to-end mode. LSTM models are well suited for time-series data and can capture some long-term dependencies, which are essential for battery SoH predictions. However, they have limitations such as long training times and a restricted ability to capture very long-term dependencies, which can affect their practical application. This is particularly relevant for SoH prediction as accurate modelling over a large number of cycles is desirable.

Recognising the limitations of LSTM models, researchers have explored more advanced architectures. Cai et al. [17] demonstrated that transformers, when combined with deep neural networks (DNNs), were more effective for battery SoH prediction. The attention mechanism in transformers allows them to assign importance to specific timesteps, thereby capturing long-term dependencies more efficiently than LSTM models. Song et al. [18] further enhanced prediction accuracy by incorporating positional and temporal encoding in transformers to predict battery RUL, addressing the challenge of capturing sequence information.

Zhang et al. [19] integrated an attention layer into a gated residual unit (GRU) architecture, combining it with particle filter information to make accurate RUL predictions. This

approach leveraged the strengths of both attention mechanisms and traditional filtering techniques, enhancing the robustness of the predictions.

Fan et al. [20] designed a gated recurrent unit–convolutional neural network (GRU-CNN) for direct SoH prediction, which combined the temporal processing capabilities of GRUs with the spatial feature extraction power of CNNs. Gu et al. [21] created a model by combining a CNN and transformer for SoH prediction. The CNN was used to incorporate time-dependent features, whereas the transformer modelled time-independent features. This hybrid approach effectively utilised different neural network architectures to enhance prediction accuracy.

Despite these advancements, previous approaches often struggle with capturing complex dependencies and require extensive computational resources for training. This study presents a novel method for modelling battery degradation and thus sheds light on a critical component of understanding this capability—interpretability of underlying stress factors—using a Temporal Fusion Transformer (TFT) [22]. The TFT model has proven to be more accurate than standard deep learning approaches for various sequence lengths. It leverages historical conditions and known future inputs to make predictions from as few as 100 input cycles. The model integrates specialised components to provide interpretability, offering insights into path-dependent degradation processes. By incorporating static metadata, our approach provides a robust solution applicable to various battery chemistries and operating conditions. This work aims to enhance the reliability and safety of BMS SoH estimation for EV and BESS applications, providing valuable insights into battery degradation processes and informing optimal management strategies.

In this study, we outline our approach, apply it to a dataset comprising over 100 cells, evaluate its performance relative to other standard neural networks, and demonstrate its potential for interpretability.

2. Framework

2.1. Dataset Description

Severson et al. [23] generated a comprehensive dataset consisting of 124 LFP/graphite cells that were cycled under fast-charging conditions, as shown in Figure 1. The C-rates for the charging and discharging protocols varied from 1C to 8C. The experiments were stopped when the batteries reached end-of-life (EOL) criteria. EOL cycle number ranged from 150 to 2300. This is subsequently referred to as the "Severson dataset". The dataset comprises three batches: batch "12-05-2017", batch "30-06-2017", and batch "12-04-2018".

Table 1 summarises key operational battery variables, including cycle number, capacity metrics, voltage/current/temperature statistics (mean, std, min, max), and depth of discharge, serving as inputs to predict future capacity.

Table 1. List of variables used in the TFT training.

Variable Description	Name	Type
Cycle number	`Cycle`	Timestep
Current capacity	`QD`	Continuous, input
Future capacity	`QD_target`	Continuous, target
Battery	`Battery`	Categorical, input
Average charging voltage	`v_c_mean`	Continuous, input
Average discharging voltage	`v_d_mean`	Continuous, input
Standard deviation of charging voltage	`v_c_std`	Continuous, input
Standard deviation of discharging voltage	`v_d_std`	Continuous, input

Table 1. *Cont.*

Variable Description	Name	Type
Depth of discharge	`dod`	Continuous, input
Average charging current	`cur_c_mean`	Continuous, input
Average discharging current	`cur_d_mean`	Continuous, input
Standard deviation of charging current	`cur_c_std`	Continuous, input
Standard deviation of discharging current	`cur_d_std`	Continuous, input
Average charging temperature	`T_c_mean`	Continuous, input
Average discharging temperature	`T_d_mean`	Continuous, input
Standard deviation of charging temperature	`T_c_std`	Continuous, input
Standard deviation of discharging temperature	`T_d_std`	Continuous, input
Minimum charging temperature	`T_c_min`	Continuous, input
Minimum discharging temperature	`T_d_min`	Continuous, input
Maximum charging temperature	`T_c_max`	Continuous, input
Maximum discharging temperature	`T_d_max`	Continuous, input

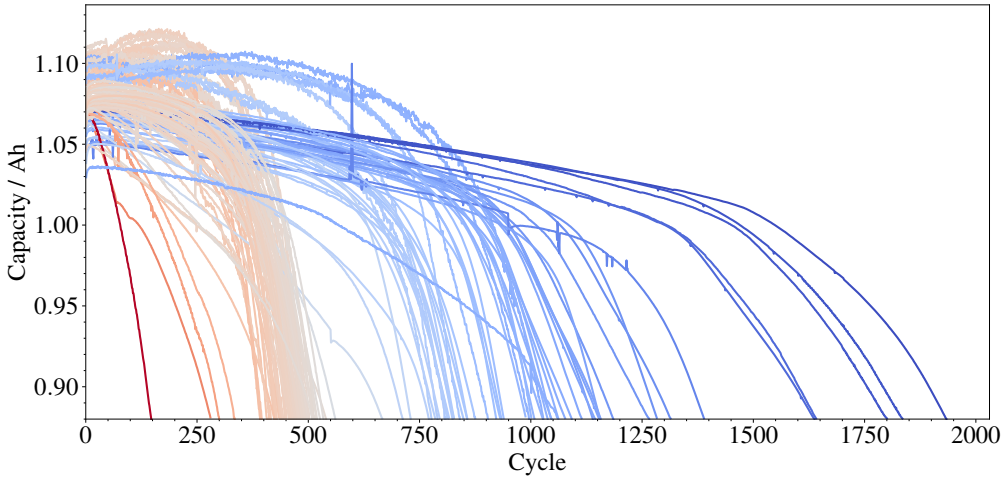

Figure 1. Capacity curves for the cells in the Severson dataset. The colour of each curve references the battery's cycle life.

2.2. Evaluation Metrics

For predicting the battery capacity curve, the average mean squared error (MSE) and mean absolute percentage error (MAPE) were calculated across the output sequence. They are defined as:

$$\text{MSE} = \frac{1}{n}\sum_{i=1}^{n}(y_i - \hat{y}_i)^2\,, \tag{1}$$

$$\text{MAPE} = \frac{1}{n}\sum_{i=1}^{n}\left|\frac{y_i - \hat{y}_i}{y_i}\right|\,, \tag{2}$$

where y_i and $\hat{y}_i$ are the true and predicted capacities at the ith output point, respectively, and n is the number of timesteps in the prediction.

2.2.1. Attention

Transformer networks make use of attention, which maps a set of queries Q and corresponding key–value pairs (K, V) to an output. For each query and each key—both of dimension d_k—we compute their dot product, scale by $\frac{1}{\sqrt{d_k}}$, and then apply a softmax

function to turn these scores into normalized weights. Those weights are used to take a weighted sum of the values (V). Formally:

$$\text{Attention}(Q, K, V) = \text{softmax}\left(\frac{QK^T}{\sqrt{d_k}}\right)V \ . \tag{3}$$

To improve the learning capacity of the model, multi-head attention is employed to increase representational power:

$$\text{MultiHead}(Q, K, V) = \text{Concat}[\text{head}_1; \text{head}_2; \ldots; \text{head}_h]W^O \ , \tag{4}$$

where

$$\text{head}_i = \text{Attention}(QW_i^Q, KW_i^K, VW_i^V) \ . \tag{5}$$

2.2.2. LSTM Layers

In time-series problems, the location of the data points within the sequence is significant. The TFT leverages local context within sequences through the use of an LSTM model, leading to performance improvement in attention-based architectures. This also serves as a replacement for more traditional positional encoding—which makes use of sine and cosine functions to produce a higher dimensional vector that includes information on the location of data within the sequence—by providing an inductive bias for the time ordering of the inputs.

The LSTM encoder is made up of cells that contain the current hidden state. As the information moves through the chain of cells, the hidden state is updated. This is controlled by three internal gates, commonly denoted as input (i), output (o), and forget (f) gates. Each gate multiplies the inputs by a weight matrix, adds a bias term, and then applies a sigmoid activation function (σ_g). The gates allow the LSTM to effectively either remember or forget different aspects of the input sequence. At time t, the equations describing the LSTM cell and gates are:

$$\begin{aligned}
f_t &= \sigma_g(W_f\, x_t + U_f\, h_{t-1} + b_f) \\
i_t &= \sigma_g(W_i\, x_t + U_i\, h_{t-1} + b_i) \\
o_t &= \sigma_g(W_o\, x_t + U_o\, h_{t-1} + b_o) \\
\tilde{c}_t &= \tanh\left(W_c\, x_t + U_c\, h_{t-1} + b_c\right) \\
c_t &= f_t \odot c_{t-1} + i_t \odot \tilde{c}_t \\
h_t &= o_t \odot \tanh c_t \ ,
\end{aligned} \tag{6}$$

where c is the cell state, h is the hidden state, W and U are weight matrices, b is the bias term. The hidden state of the final encoder cell is passed to the next layer in the model.

2.2.3. Variable Selection

The model uses three types of input: past inputs, known future inputs, and static metadata. Each input is initially passed through a variable selection network. This involves transforming the inputs before passing them through a Gated Residual Network (GRN) [22]. Linear transformations are used for continuous variables and entity embeddings [24] are used for the categorical variables. The GRN allows some inputs to skip layers of the network. This enhances the model's ability to deal with noisy inputs, and prevents the network from becoming too complex. Specifically, the GRN operation is given by:

$$GRN_\omega(\boldsymbol{a}, \boldsymbol{c}) = \text{LayerNorm}(\boldsymbol{a} + GLU_\omega(\boldsymbol{\eta}_1)) \ , \tag{7}$$

with the intermediate dense layers $\boldsymbol{\eta}_1$ and $\boldsymbol{\eta}_2$ given by:

$$\begin{aligned} \boldsymbol{\eta}_1 &= \boldsymbol{W}_{1,\omega}\boldsymbol{\eta}_2 + \boldsymbol{b}_{1,\omega} \\ \boldsymbol{\eta}_2 &= ELU(\boldsymbol{W}_{2,\omega}\boldsymbol{a} + \boldsymbol{W}_{3,\omega}\boldsymbol{c} + \boldsymbol{b}_{2,\omega}) \, , \end{aligned} \tag{8}$$

where $\boldsymbol{a}$ is the primary input, $\boldsymbol{c}$ is a context vector, ELU is the the Exponential Linear Unit activation function [25].

The variable selection network takes the transformed inputs, represented by $\Xi_t = \left[\tilde{\varsigma}_t^{(1)^T}, ..., \tilde{\varsigma}_t^{(m_\chi)^T}\right]^T$, where $\tilde{\varsigma}_t^{(j)}$ is the transformed input of the jth variable at time t. Ξ_t is passed into the variable selection network along with an external context vector $\boldsymbol{c}_s$, and the result is passed through a softmax function:

$$\boldsymbol{\nu}_{\chi t} = \text{Softmax}(GRN\nu_\chi(\Xi_t, \boldsymbol{c}_s)); . \tag{9}$$

$\boldsymbol{\nu}_{\chi t}$ is the resulting vector of variable selection weights at time t, with each element indicating the model's learned importance for a corresponding input variable at that time step. These weights are then used to compute a weighted combination of the inputs at each time step, enabling the model to dynamically adjust its focus to the most relevant features throughout the sequence.

To quantify overall variable importance, the weights $\boldsymbol{\nu}_{\chi t}$ are extracted at inference time across all time steps and averaged temporally. These average weights are then further averaged across the five test cells to yield a single importance score for each variable.

In this way, the model's learned attentional focus over time and across different test cases is summarised by interpretable importance scores. This is explored further in Section 2.3.

2.3. Interpretability

Temperature Effect

A study of the model's interpretability is presented in Section 3.4. To do this, test cells which had irregular behaviour in a particular variable were used. Then, the variable importance scores were measured to assess whether the model accounted for that variable's impact on the degradation. The most obvious choice for this variable was temperature.

The effect of temperature on battery degradation is well studied. The exact implications of operating temperature depend on the dominant ageing mechanism; however, temperatures over 25 °C generally leads to accelerated ageing, due to increased reaction rates within the cell [26]. The description of temperature dependency of chemical reactions is given by the Arrhenius equation:

$$r = A \, \exp\left(-\frac{E_a}{k_B T}\right) , \tag{10}$$

where E_a is the activation energy, k_B is the Boltzmann constant, T is the absolute temperature, and A is a pre-exponential factor.

3. Results

To evaluate the model's performance, a prediction of the cell's capacity curve was performed. The results are shown in Table 2.

Table 2. Performance comparison of different models for varying sequence lengths.

Model	100I, 400O		200I, 400O		200I, 600O	
	MAPE	**MSE**	**MAPE**	**MSE**	**MAPE**	**MSE**
CNN	1.12	2.82	0.87	1.73	0.89	1.86
LSTM	1.38	3.84	0.87	2.07	1.02	2.07
Transformer	1.43	3.95	1.02	2.54	1.40	3.35
Our model	0.67	1.52	0.37	0.41	0.68	1.83

3.1. Variables

The training variables for the model were intentionally selected for ease of calculation, with all continuous variables determined on a per-cycle basis. This approach simplifies the model's deployment in real-world scenarios. The variables are listed in Table 1.

3.2. Training Procedure

For the experiments, the dataset was partitioned into training, test, and validation splits, with five cells reserved for testing, five for validation, and the remaining cells used for training. This allocation balanced the need for sufficient training diversity with reliable model selection and evaluation. The validation and test cells were selected to reflect a representative range of initial capacities and cycling conditions. All experiments were run on a single Nvidia V100 GPU. Each epoch took approximately 50 s to train, and each model was trained for a maximum of 30 epochs. Hyperparameter optimisation was conducted via random search, scanning over a grid of predefined parameters as defined in Table 3:

Table 3. Search values for each hyperparameter used in the optimisation.

Hyperparameter	Values
Dropout rate	[0.1, 0.2, 0.3, 0.4, 0.5, 0.7, 0.9]
Hidden layer Size	[10, 20, 40, 80]
Minibatch size	[64, 128, 256]
Learning rate	[0.0001, 0.001, 0.01]
Max. gradient norm	[0.01, 1.0, 100.0]
Num. heads	[1, 4]

One test condition is displayed in Section 3.3. Further testing conditions (different permutations of train/test/validation splits) are displayed in Appendix B.

3.3. Model Accuracy Results

The proposed method was compared to a range of conventional data-driven techniques to provide accuracy benchmarks. To do this, the data were split up into the standard train/test/validation groupings. Six cells were reserved for testing, six for validation, and the remainder were used for training. Early stopping was used to avoid overtraining. Three different permutations of train/test/validation were tested in total (results for the last two are presented in Appendix B). To assess the ability of the model to perform over a variety of context windows, three different combinations of varying input/output length were chosen. The details of each experiment are summarised in Table 4.

When evaluated using the Severson dataset, the model demonstrated substantial performance improvements. Unlike purely physics-based methods, the model does not require any prior electrochemical knowledge of the battery cell. Additionally, by incorporating battery type and capacity as static inputs (metadata), the model enables the training of a generalized model on datasets that include degradation data from various cells. This

allows the model to leverage shared knowledge from similar degradation patterns across different cells. An example of the model's capacity prediction for two cells is shown in Figure 2, additional plots are shown in Appendix B.2.

Table 4. Input and output sequence length configurations for each permutation setting.

Permutation	Input Length	Output Length
1	100	400
2	100	400
3	100	400
1	200	400
2	200	400
3	200	400
1	200	600
2	200	600
3	200	600

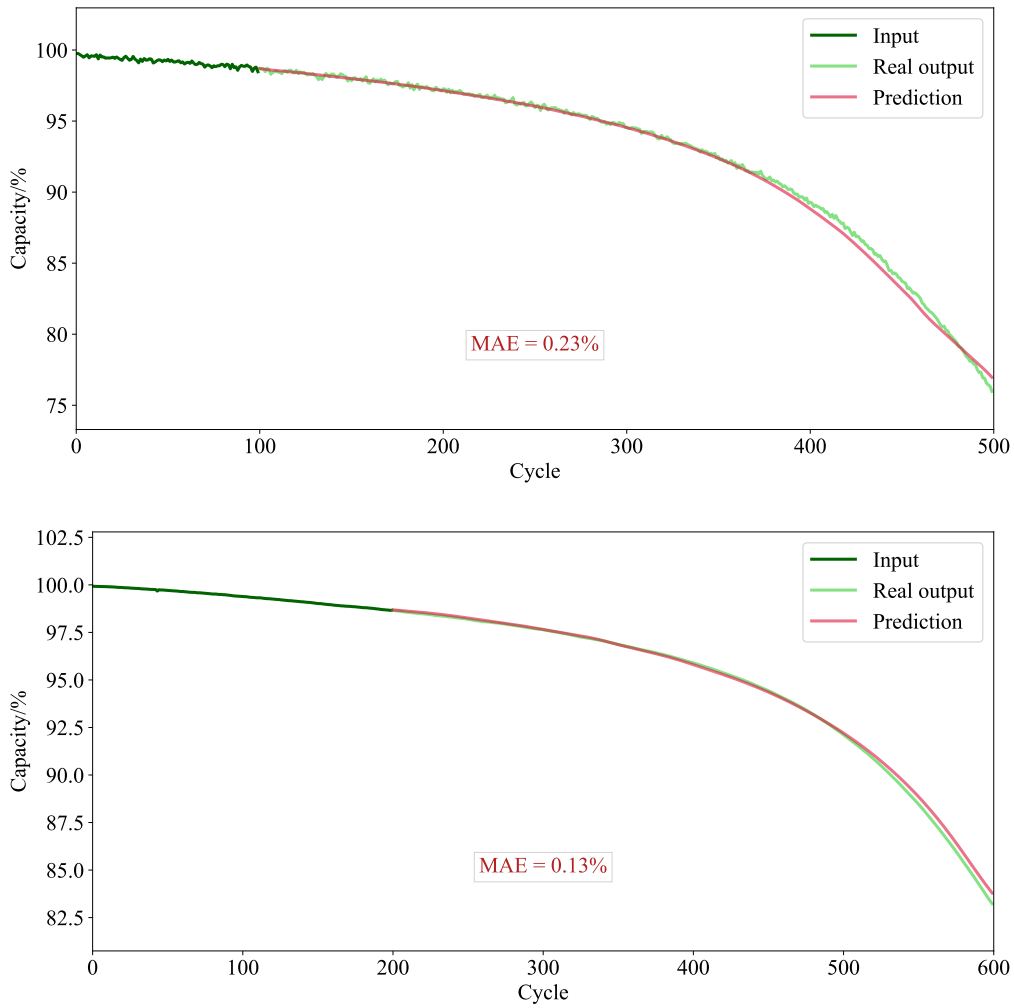

Figure 2. Predicted capacity from the trained TFT for 400 cycles of two cells. The mean absolute error for the prediction is displayed.

Interestingly, as the input length increased from 100 cycles to 200 cycles (while keeping the output length fixed at 400), both the MAPE and MSE worsened, indicating a decrease in performance. Several factors may explain this. First, the LSTM input encoder and self-attention layers, which have a complexity of $O(n^2)$ with respect to input length [27], may cause bottlenecks during training. Second, this suggests that the most recent input timesteps are generally more influential. The model may become "distracted" by earlier timesteps, leading to overfitting and decreased accuracy as the input length grows.

However, as shown in Table 2, when the output length was increased to 600 cycles, the model outputs remained accurate compared to the benchmarks.

3.4. Interpretability

Having established the accuracy of the model, we now demonstrate how relationships between the data that lead to predictions can be interpreted. While some conventional data-driven techniques can produce accurate results, the relative contributions of each of the potentially many features to the overall degradation remain unknown. Variable selection considers both static and time-dependent covariates, quantifying the impact of each feature per instance and filtering out unnecessary, noisy inputs.

The Severson dataset was used to investigate the usefulness of the model's variable importance scores. To do this, outlier cells in specific variables were used; these are referred to as "importance test cells". For example, a cell with a relatively high charging temperature could be used, as it is expected that the degradation of this cell would be more strongly affected by the charging temperature compared with an average cell. By calculating the variable importance score for this cell and comparing it with the average scores across the dataset, we can assess the model's ability to make realistic estimates. If the charging temperature's importance score for the test cell exceeds the average, it suggests that the model accurately reflects the relative importance of that variable.

Figure 3 shows the variable importance weights for the whole Severson dataset. As expected, the cycle number, i.e., the age of the cell, was the most important factor affecting the degradation. The second and third most important variables were both temperature variables, which is also sensible.

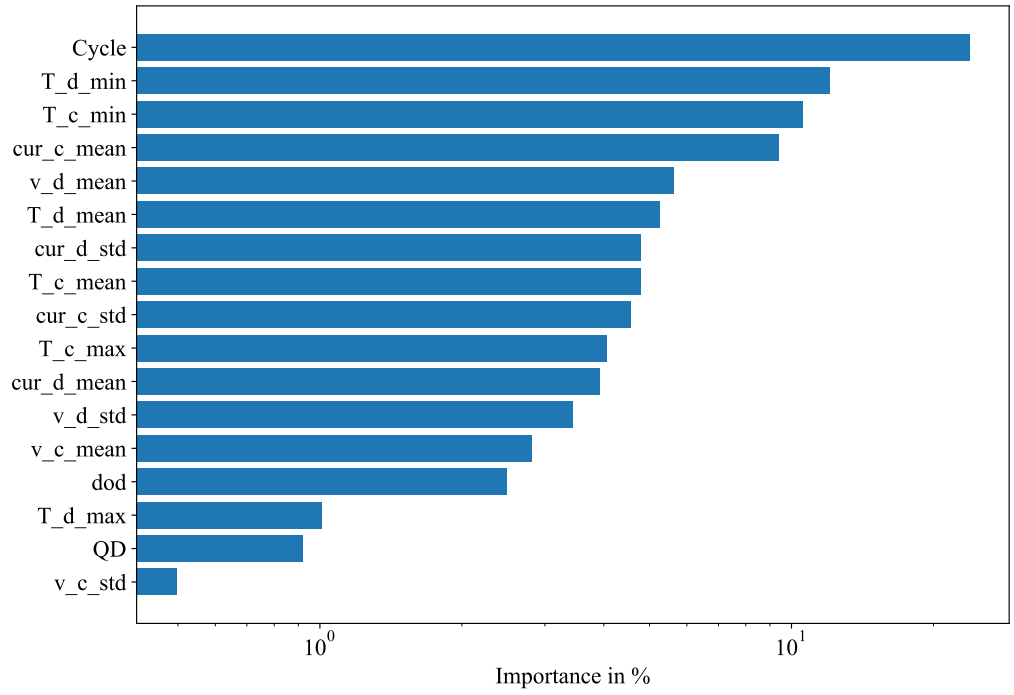

Figure 3. Average variable importance weights for all cells.

Several test cases were identified for studying variable importance. Here, we present importance test cell 2 as an example, and others are shown in Appendix A. The charging temperature for that cell was much higher than average, as shown in Figure 4. The corresponding attention scores for that cell are shown in Figure 5. Comparing this with Figure 3 demonstrates that the test cell had a higher attention score for the mean charging temperature (labelled `T_c_mean`) than the average score for the whole dataset. The cell's attention score for that variable was 5.48%, making it the fifth most important variable; whereas the average score was 4.79%, which ranked as the eighth most important variable. In this way, the model can correctly assign a higher importance where a particular feature plays a greater role in the cell's degradation.

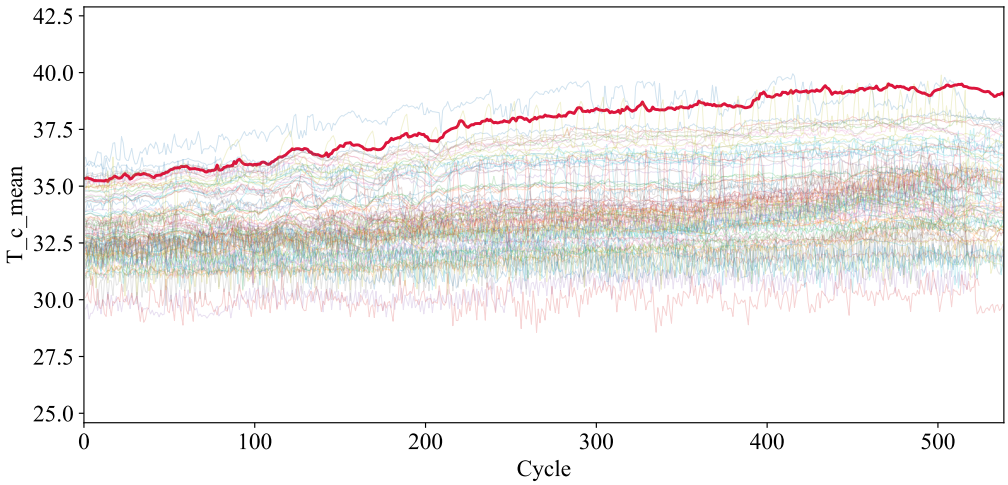

Figure 4. Minimum charging temperature for importance test cell 2 (red line) compared with all other cells in the dataset, showing that the chosen cell is higher than average in this variable.

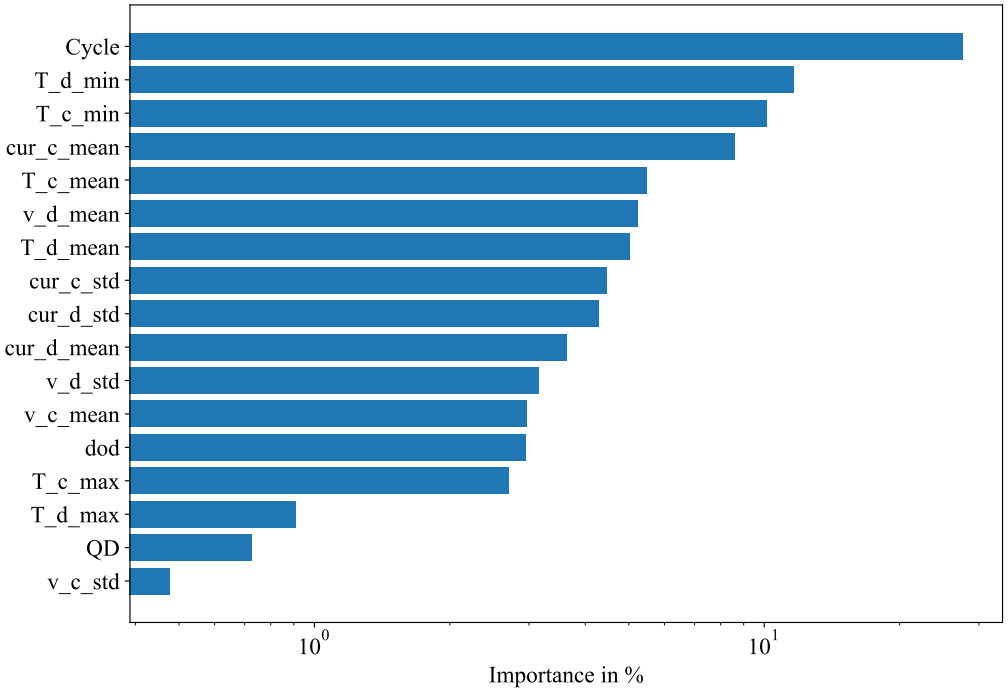

Figure 5. Variable importance weights for importance test cell 2.

4. Conclusions

This study presented a novel approach for modelling battery degradation using a Temporal Fusion Transformer. The proposed model demonstrated superior accuracy compared to standard deep learning methods across various sequence lengths. The mean absolute error for the predicted capacity curve was found to be between 0.67% and 0.85%, compared with 0.87–1.40% for the benchmark models.

The model effectively integrates both continuous and categorical inputs, which can be either static or time-varying. In addition, it offers interpretable outputs, yielding valuable insights into specific factors that impact a given battery's degradation. This could enable a user to extend the life of a battery during operation. Moreover, the model is capable of accurately forecasting degradation curves with as few as 100 input cycles.

The model presented in this study has great potential to enhance the reliability and safety of lithium-ion batteries in electric vehicles or energy storage systems. Moreover, the model is agnostic to cell chemistry and can be readily applied to other battery types, provided that suitable training data are available.

Author Contributions: Conceptualization, J.S.; Methodology, J.S.; Software, J.S. and R.M.; Formal analysis, J.S. and R.M.; Investigation, J.S. and R.M.; Writing—original draft, J.S. and R.M.; Writing—review & editing, K.U.; Visualization, R.M.; Supervision, K.U.; Project administration, K.U. All authors have read and agreed to the published version of the manuscript.

Funding: This research received no external funding.

Data Availability Statement: The dataset used in this study is publicly available at https://data.matr.io/1/ (accessed on 10 February 2024).

Acknowledgments: We express our gratitude to Envision Energy for supplying the R&D resources that made this work possible.

Conflicts of Interest: Authors James Sadler, Rizwaan Mohammed and Kotub Uddin were employed by the company Envision Energy UK COE Ltd. All authors declare that the research was conducted in the absence of any commercial or financial relationships that could be construed as a potential conflict of interest.

Abbreviations

The following abbreviations are used in this manuscript:

Ah	Ampere-hour
BESS	Battery Energy Storage System
BMS	Battery Management System
CNN	Convolutional Neural Network
C-rate	Charge/Discharge Rate
DoD	Depth of Discharge
DNN	Deep Neural Network
ELU	Exponential Linear Unit
EOL	End of Life
EV	Electric Vehicle
GRN	Gated Residual Network
GRU	Gated Recurrent Unit
IRR	Internal Rate of Return
LFP	Lithium Iron Phosphate
LSTM	Long Short-Term Memory
LCOS	Levelised Cost of Storage
MAPE	Mean Absolute Percentage Error
MSE	Mean Squared Error

NN	Neural Network
NMC	Nickel Manganese Cobalt
PF	Particle Filter
ReLU	Rectified Linear Unit
RUL	Remaining Useful Life
SoC	State of Charge
SoH	State of Health
SVM	Support Vector Machine
TFT	Temporal Fusion Transformer
Q, K, V	Query, Key, Value (in attention mechanism)

Appendix A. Additional Variable Importance Results

Figure 3 shows the average attention weights over the whole dataset. Section 3.4 showed an example of a cell with a high charging temperature and a correspondingly high attention score for that variable. Other examples are shown below.

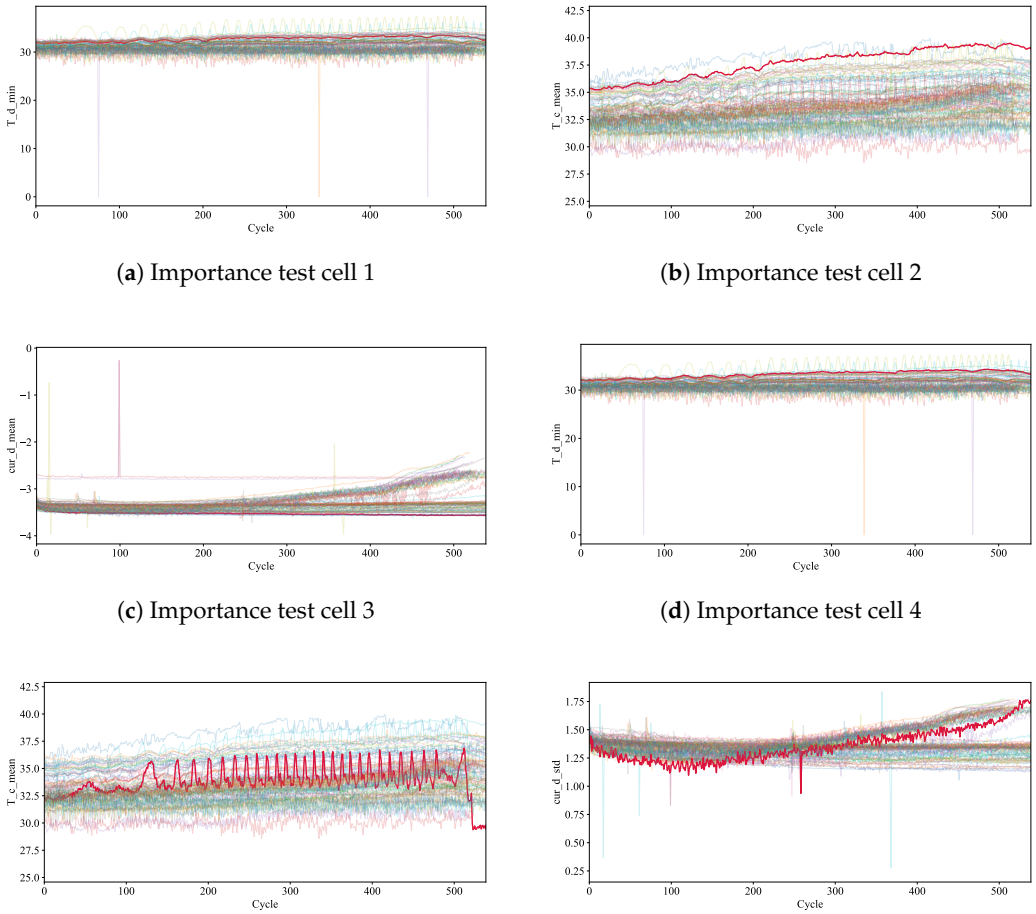

(**a**) Importance test cell 1

(**b**) Importance test cell 2

(**c**) Importance test cell 3

(**d**) Importance test cell 4

(**e**) Importance test cell 5

(**f**) Importance test cell 6

Figure A1. The six test cells used for the variable importance study are shown. For each cell, the particular variable is plotted with the test cell shown as a red line and the other cells in the sample shown as lighter coloured lines. This demonstrates that each test cell is an outlier in its respective variable.

Table A1. Additional test cells for variable importance study. The importance score for the chosen variable is shown along with the average importance score for that variable over the whole dataset.

Cell	Variable	Average Score/%	Cell Score/%
Importance test cell 1	Min discharge temperature	12.03	13.14
Importance test cell 2	Mean charge temperature	4.79	5.48
Importance test cell 3	Mean discharge current	3.92	4.90
Importance test cell 4	Min discharge temperature	12.03	13.54
Importance test cell 5	Mean charge temperature	4.79	5.59
Importance test cell 6	Std. dev. discharge current	4.79	5.42

Appendix B. Additional Accuracy Results

Accuracy results from other permutations of train/test splits.

Appendix B.1. Test Condition 2

Table A2. Comparison of results of various approaches using 100 input cycles and 400 output cycles—test condition 2.

Model	MAPE	MSE
CNN	1.27	4.08
LSTM	1.81	5.94
Transformer	1.75	5.37
Our model	0.65	1.40

Table A3. Comparison of results of various approaches using 200 input cycles and 400 output cycles—test condition 2.

Model	MAPE	MSE
CNN	1.01	2.36
LSTM	1.24	3.76
Transformer	1.22	3.74
Our model	0.75	1.49

Table A4. Comparison of results of various approaches using 200 input cycles and 600 output cycles—test condition 2.

Model	MAPE	MSE
CNN	1.10	2.99
LSTM	1.26	3.04
Transformer	1.43	3.25
Our model	0.67	0.71

Appendix B.2. Test Condition 3

Table A5. Comparison of results of various approaches using 100 input cycles and 400 output cycles—test condition 3.

Model	MAPE	MSE
CNN	1.29	4.21
LSTM	1.73	5.30
Transformer	1.21	3.40
Our model	0.84	1.46

Table A6. Comparison of results of various approaches using 200 input cycles and 400 output cycles—test condition 3.

Model	MAPE	MSE
CNN	1.14	3.52
LSTM	1.22	3.57
Transformer	1.17	2.32
Our model	0.57	1.29

Table A7. Comparison of results of various approaches using 200 input cycles and 600 output cycles—test condition 3.

Model	MAPE	MSE
CNN	1.16	3.11
LSTM	1.22	3.19
Transformer	1.13	2.90
Our model	0.71	2.62

Appendix C. Additional Visualisations

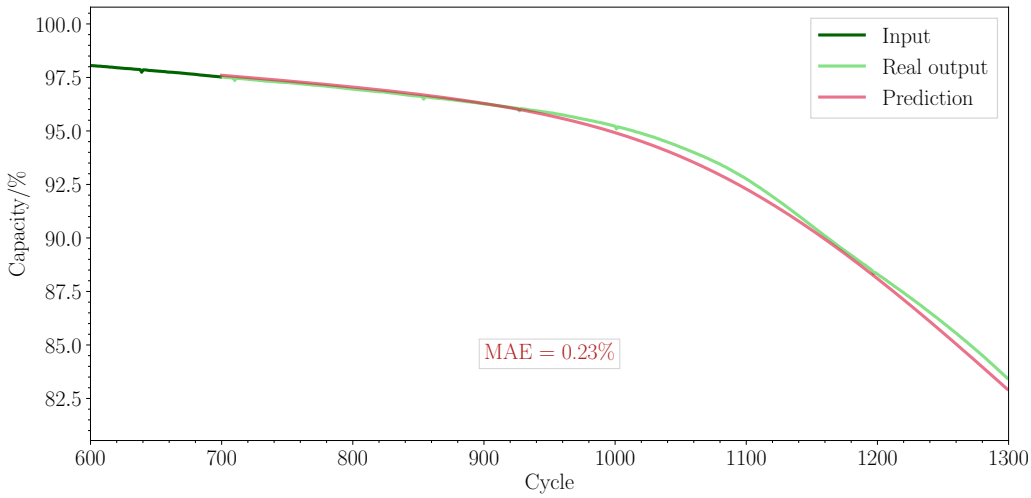

Figure A2. Predicted capacity from 100 inputs of cycles in later life for test cell 3.

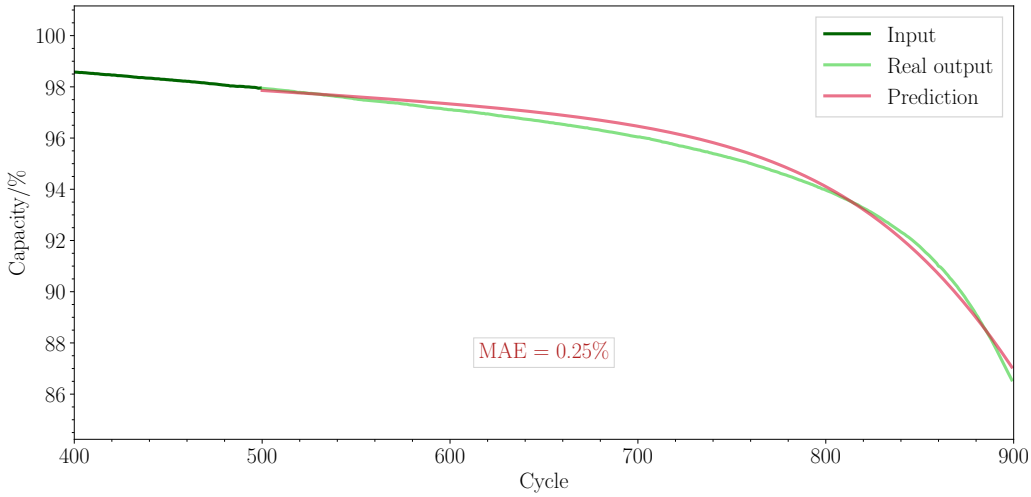

Figure A3. Predicted capacity from 100 inputs of cycles in later life for test cell 4.

References

1. Liu , Q.; Chen, G. Design of Electric Vehicle Battery Management System. *J. Phys. Conf. Ser.* **2023**, *2614*, 012001. [CrossRef]
2. Habib, A.K.M.A.; Hasan, M.K.; Issa, G.F.; Singh, D.; Islam, S.; Ghazal, T.M. Lithium-Ion Battery Management System for Electric Vehicles: Constraints, Challenges, and Recommendations. *Batteries* **2023**, *9*, 152. [CrossRef]
3. Kassim, M.R.M.; Jamil, W.A.W.; Sabri, R.M. State-of-Charge (SOC) and State-of-Health (SOH) Estimation Methods in Battery Management Systems for Electric Vehicles. In Proceedings of the 2021 IEEE International Conference on Computing (ICOCO), Guadalajara, Mexico, 20–22 October 2021; pp. 91–96. [CrossRef]
4. Barré, A.; Deguilhem, B.; Grolleau, S.; Gérard, M.; Suard, F.; Riu, D. A Review on Lithium-Ion Battery Ageing Mechanisms and Estimations for Automotive Applications. *J. Power Sources* **2013**, *241*, 680–689. [CrossRef]
5. Uddin, K.; Perera, S.; Widanage, W.D.; Somerville, L.; Marco, J. Characterising Lithium-Ion Battery Degradation through the Identification and Tracking of Electrochemical Battery Model Parameters. *Batteries* **2016**, *2*, 13. [CrossRef]
6. Mowri, S.; Barai, A.; Moharana, S.; Gupta, A.; Marco, J. Assessing the Impact of First-Life Lithium-Ion Battery Degradation on Second-Life Performance. *Energies* **2024**, *17*, 501. [CrossRef]
7. Lin, W.-J.; Chen, K.-C. Evolution of Parameters in the Doyle-Fuller-Newman Model of Cycling Lithium-Ion Batteries by Multi-Objective Optimization. *Appl. Energy* **2022**, *314*, 118925. [CrossRef]
8. Dubarry, M.; Beck, D. Perspective on Mechanistic Modeling of Li-Ion Batteries. *Acc. Mater. Res.* **2022**, *3*, 843–853. [CrossRef]
9. Uddin, K.; Somerville, L.; Barai, A.; Lain, M.; Ashwin, T.; Jennings, P.; Marco, J. The Impact of High-Frequency-High-Current Perturbations on Film Formation at the Negative Electrode-Electrolyte Interface. *Electrochim. Acta* **2017**, *233*, 1–12. [CrossRef]
10. Dong, H.; Jin, X.; Lou, Y.; Wang, C. Lithium-Ion Battery State of Health Monitoring and Remaining Useful Life Prediction Based on Support Vector Regression-Particle Filter. *J. Power Sources* **2014**, *271*, 114–123. [CrossRef]
11. Vetter, J.; Novák, P.; Wagner, M.; Veit, C.; Möller, K.-C.; Besenhard, J.; Winter, M.; Wohlfahrt-Mehrens, M.; Vogler, C.; Hammouche, A. Ageing Mechanisms in Lithium-Ion Batteries. *J. Power Sources* **2005**, *147*, 269–281. [CrossRef]
12. Li, X.; Ju, L.; Geng, G.; Jiang, Q. Data-Driven State-of-Health Estimation for Lithium-Ion Battery Based on Aging Features. *Energy* **2023**, *274*, 127378. [CrossRef]
13. Feng, H.; Shi, G. SOH and RUL Prediction of Li-Ion Batteries Based on Improved Gaussian Process Regression. *J. Power Electron.* **2021**, *21*, 1845–1854. [CrossRef]
14. Feng, R.; Wang, S.; Yu, C.; Hai, N.; Fernandez, C. High Precision State of Health Estimation of Lithium-Ion Batteries Based on Strong Correlation Aging Feature Extraction and Improved Hybrid Kernel Function Least Squares Support Vector Regression Machine Model. *J. Energy Storage* **2024**, *90*, 111834. [CrossRef]
15. Zhang, Y.; Xiong, R.; He, H.; Pecht, M.G. Long Short-Term Memory Recurrent Neural Network for Remaining Useful Life Prediction of Lithium-Ion Batteries. *IEEE Trans. Veh. Technol.* **2018**, *67*, 5695–5705. [CrossRef]
16. Li, P.; Zhang, Z.; Grosu, R.; Deng, Z.; Hou, J.; Rong, Y.; Wu, R. An End-to-End Neural Network Framework for State-of-Health Estimation and Remaining Useful Life Prediction of Electric Vehicle Lithium Batteries. *Renew. Sustain. Energy Rev.* **2022**, *156*, 111843. [CrossRef]
17. Cai, Y.; Li, W.; Zahid, T.; Zheng, C.; Zhang, Q.; Xu, K. Early Prediction of Remaining Useful Life for Lithium-Ion Batteries Based on CEEMDAN-Transformer-DNN Hybrid Model. *Heliyon* **2023**, *9*, e17754. [CrossRef]
18. Song, W.; Wu, D.; Shen, W.; Boulet, B. A Remaining Useful Life Prediction Method for Lithium-Ion Battery Based on Temporal Transformer Network. *Procedia Comput. Sci.* **2023**, *217*, 1830–1838. [CrossRef]
19. Zhang, J.; Huang, C.; Chow, M.-Y.; Li, X.; Tian, J.; Luo, H.; Yin, S. A Data-Model Interactive Remaining Useful Life Prediction Approach of Lithium-Ion Batteries Based on PF-BiGRU-TSAM. *IEEE Trans. Ind. Inform.* **2024**, *20*, 1144–1154. [CrossRef]
20. Fan, Y.; Xiao, F.; Li, C.; Yang, G.; Tang, X. A Novel Deep Learning Framework for State of Health Estimation of Lithium-Ion Battery. *J. Energy Storage* **2020**, *32*, 101741. [CrossRef]
21. Gu, X.; See, K.; Li, P.; Shan, K.; Wang, Y.; Zhao, L.; Lim, K.C.; Zhang, N. A Novel State-of-Health Estimation for the Lithium-Ion Battery Using a Convolutional Neural Network and Transformer Model. *Energy* **2023**, *262*, 125501. [CrossRef]
22. Lim, B.; Arık, S.Ö.; Loeff, N.; Pfister, T. Temporal Fusion Transformers for Interpretable Multi-Horizon Time Series Forecasting. *Int. J. Forecast.* **2021**, *37*, 1748–1764. [CrossRef]
23. Severson, K.A.; Attia, P.M.; Jin, N.; Perkins, N.; Jiang, B.; Yang, Z.; Chen, M.H.; Aykol, M.; Herring, P.K.; Fraggedakis, D.; et al. Data-Driven Prediction of Battery Cycle Life Before Capacity Degradation. *Nat. Energy* **2019**, *4*, 383–391. [CrossRef]
24. Gal, Y.; Ghahramani, Z. A Theoretically Grounded Application of Dropout in Recurrent Neural Networks. In *Advances in Neural Information Processing Systems*; Lee, D., Sugiyama, M., Luxburg, U., Guyon, I., Garnett, R., Eds.; Curran Associates, Inc.: Nice, France, 2016; Volume 29. Available online: https://proceedings.neurips.cc/paper_files/paper/2016/file/076a0c97d09cf1a0ec3e19c7f2529f2b-Paper.pdf (accessed on 3 June 2024).
25. Clevert, D.-A.; Unterthiner, T.; Hochreiter, S. Fast and Accurate Deep Network Learning by Exponential Linear Units (ELUs). *arXiv* **2015**, arXiv:1511.07289.

26. Kucinskis, G.; Bozorgchenani, M.; Feinauer, M.; Kasper, M.; Wohlfahrt-Mehrens, M.; Waldmann, T. Arrhenius Plots for Li-Ion Battery Ageing as a Function of Temperature, C-Rate, and Ageing State–An Experimental Study. *J. Power Sources* **2022**, *549*, 232129. [CrossRef]
27. Vaswani, A.; Shazeer, N.; Parmar, N.; Uszkoreit, J.; Jones, L.; Gomez, A.N.; Kaiser, Ł.; Polosukhin, I. Attention Is All You Need. *Adv. Neural Inf. Process. Syst.* **2017**, *30*, 5998–6008.